Identifying the facet-dependent active sites of Cu_2O for selective C-N coupling toward electrocatalytic urea synthesis

Jiamin Zhao [a,b], Ying Yuan [a], Fei Zhao [c], Wei Han [d], Qing Yuan [a], Meimei Kou [a], Jinsheng Zhao [a,*], Chen Chen [b,*], Shuangyin Wang [b,*]

[a] School of Chemistry and Chemical Engineering, Liaocheng University, Liaocheng 252059, China
[b] State Key Laboratory of Chemo/Bio-Sensing and Chemometrics, College of Chemistry and Chemical Engineering, Advanced Catalytic Engineering Research Center of the Ministry of Education, Hunan University, Changsha 410000, China
[c] College of Chemistry and Chemical Engineering, Taishan University, Taian 271000, China
[d] National Energy R&D Center for Petroleum Refining Technology, Research Institute of Petroleum Processing, SINOPEC, 18 Xue Yuan Road, Beijing 100083, China

ARTICLE INFO

ABSTRACT

Understanding the activity phases and reaction mechanisms at the atomic level is essential for the design of electrocatalysts. Herein we investigate the origin of the facet-dependent activity of model Cu_2O catalyst for C-N coupling toward electrocatalytic urea synthesis. It was found that the activity of urea synthesis depends on the crystalline facets of Cu_2O. The Cu_2O (100) facet exhibits higher urea activity and selectivity than the (110) facet, with an average urea yield of 62.4 mmol$\cdot$g$^{-1}\cdot$h^{-1} at –1.5 V (RHE). By using Raman, UV–vis and XPS techniques, it was observed that Cu^+ serves as active sites at (100) face of Cu_2O, which promotes C-N coupling through synergistic interaction with Cu^0. Furthermore, the combined results of operando ATR-SEIRAS and DFT calculations demonstrate that the Cu-Cu_2O (100) facet facilitates electrocatalytic C-N coupling between *CO and *NH intermediates due to the reduced energy barriers of hydrogenated *NO on the Cu-Cu_2O (100) facet.

1. Introduction

Urea is a versatile and foundational nitrogen fertilizer for increasing crop productivity [1]. However, the industrial urea production process is still the energy-intensive Haber-Bosch process, which consumes approximately 2 % of global energy and leads to 1.44 % of global carbon dioxide emissions [2–6]. Thus, the urea electrosynthesis route is becoming a noteworthy trend through the use of clean and renewable energy sources [7–14]. Among them, the electrocatalytic coupling of NO_3^- with CO_2 has attracted attention as a promising route for urea synthesis given the advantage of much lower bond energy of N$=$O bond (204 kJ mol^{-1}) than that of N$\equiv$N triple bond (941 kJ mol^{-1}) [15,16] (Fig. S1). This process can not only convert low-value CO_2 to high-value urea by electrocatalysis, but also effectively treat nitrogen-containing wastewater, protect the environment, and reform the urea industry at the same time [17].

Generally, electrocatalytic urea synthesis includes not only C-N coupling reactions, but also more multi-step proton-coupled electron transfer processes, as well as various reactive intermediates [11,18,19]. However, these reactive intermediate species are also highly susceptible to various side reactions, mainly including NO_3^- reduction (NO3RR), carbon dioxide reduction (CO2RR), the hydrogen evolution reaction (HER), and the generation of other amide products at negative potentials, which hinder the efficient synthesis of urea [20,21]. Therefore, the search for active sites to improve the efficiency of C-N coupling in electrocatalytic urea synthesis plays a key role in electrocatalytic urea synthesis [22]. In this regard, our group designed CeO_2 enriched with oxygen vacancies in which the vacancies can stabilize the crucial intermediates of *NO and then improve the selectivity and efficiency of C-N coupling instead of protonation [23]. In addition, Fe-Ni diatomic catalysts with a "trinity" of active site, activation site and coupling site were designed as efficient urea electrosynthesis sites, achieving high urea yields of 20.2 mmol$\cdot$h$^{-1}\cdot$g^{-1} [24]. Recently, Cu_1-CeO_2 catalysts were fabricated and it was shown that the Cu_4 cluster was the real active sites for the C-N coupling reaction [25]. Until now, we have further confirmed that Cu-based catalysts have the optimal C-N coupling performance among the many active sites [26]. The research interest has gradually shifted to the optimal redesign of Cu-based catalysts to enhance the C-N coupling reaction.

Herein, Cu_2O was selected as a model catalyst due to its flexible and

---

* Corresponding authors.
E-mail addresses: j.s.zhao@163.com (J. Zhao), chenc@hnu.edu.cn (C. Chen), shuangyinwang@hnu.edu.cn (S. Wang).

adjustable crystal surface structure. Firstly, high urea yields were found at specific active sites on the Cu_2O (100) face, with an average urea yield of 62.4 mmol·g^{-1}·h^{-1} at –1.5 V (RHE), exceeding most previous reports. Then, the structural evolution during the electrocatalytic reaction was characterized by Raman, UV–vis, and XPS, revealing Cu^0/Cu^+ as the active site for C-N coupling. Finally, the C-N coupling mechanism was identified by operando ATR-SEIRAS spectroscopy and in-situ Raman. In conclusion, we identified the active sources and pathways of C-N coupling reactions on model Cu_2O catalysts, providing insight into urea synthesis and theoretical guidance for the development of urea electrosynthesis and industrial applications of organic electrosynthesis.

2. Experimental

2.1. Materials synthesis

The facet-dependent Cu_2O nanoparticles (NCs) were prepared by hydroxylamine hydrochloride reduction method by altering the proportion of precursors. Typically, 89.2, 83.4, and 69.2 mL of ultrapure water were added to round-bottom flasks labeled a, b, and c, respectively. Then, 5 mL of 0.1 M $CuCl_2$ solution and 0.87 g of SDS powder were added to each sample flask and sonicated for 10 min to completely dissolve the SDS powder, followed by the addition of 1.8 mL of 1.0 M NaOH solution, and the resulting solution immediately turned light blue. Next, 4.0, 9.8 and 24 mL of 0.1 M $NH_2OH·HCl$ were quickly injected into vials a, b and c, respectively, and kept in a water bath at 35 °C for 1 h. Finally, the products were centrifuged, washed, and vacuum dried.

Synthesis of cubic Cu_2O with tunable size. To synthesize 45 nm cubic Cu_2O (c-Cu_2O-45 NCs), 400 mL of ultrapure water was placed in a water bath at 55 °C for 30 min, then 1 mL of aqueous $CuSO_4$ solution (1.2 mol L^{-1}) was quickly added and stirred for 20 min, followed by adding 1 mL of aqueous NaOH solution (4.8 mol L^{-1}) drop by drop to this solution and stirring for 20 min. After that, 1 mL of aqueous ascorbic acid solution (1.2 mol L^{-1}) was added and kept for 3 h. Finally, the samples were obtained by centrifugation, washing and vacuum drying. 69 nm cubic Cu_2O (c-Cu_2O-69 NCs) was synthesized similarly, except that 0.26 g sodium citrate was added to the initial 400 mL deionized water at 55 °C.

2.2. Materials characterization

Transmission electron microscopy (TEM) was performed on a Tecnai G2 F20 microscope with an accelerating voltage of 200 kV. SEM measurement was obtained on an XL30 ESEM FEG scanning electron microscope at an accelerating voltage of 20 kV. X-ray photoelectron spectroscopy (XPS) was determined on a VG ESCALAB MK2 spectrometer equipped with an excitation source of Al Kα X-rays at 12.5 kV and 250 W. X-ray diffraction (XRD) was recorded at $10° \le 2\theta \le 80°$ by Empyrean powder X-ray diffractometer equipped with Cu Kα radiation at 40 kV and 200 mA. Raman spectroscopy was performed on a Renishaw InVia Reflex Raman instrument to characterize the structure of Cu_2O with an excitation wavelength of 632 nm. UV–vis absorption spectroscopy was performed on a JASCO V-670 spectrophotometer. The reacted samples need to be pre-treated by vacuum drying at 80 °C before characterization.

2.3. Electrochemical performance test

The H-cell configuration consists of a working electrode, an Ag/AgCl electrode, a Nafion 117 membrane (Dupont), and a carbon rod anode. The CHI 630E electrochemical workstation was used in the electrochemical tests. The Nafion membranes require pretreatment before use. First, the Nafion membranes were placed in 5 % H_2O_2 for 1 h at 80 °C; then sonicated in ultrapure water for 30 min. The electrode solution consisted of 0.1 M $KHCO_3$ and 50 mM $NaNO_3$. The working electrode was prepared as follows: 2 mg of catalyst was dispersed in 475 μL of

isopropanol solution and 25 μL of Nafion (5 wt% aqueous solution) and then sonicated for 40 min to form a homogeneous ink. Note that ice needs to be added during this process to prevent Nafion polymerizing. After that, 25 μL of catalyst ink was uniformly loaded on carbon paper (Hesen, 1.0 *0.5 cm^2) and dried naturally to obtain a working electrode. Prior to the electrochemical experiments, the cathodic electrolyte was fed with carbon dioxide for 30 min at a flow rate of 30 mL min^{-1}. Electrochemical experiments were performed using the chronoamperometric method, with each electrolysis test performed at each potential for 0.5 h. The applied potentials were measured for the Ag/AgCl reference electrode and were calculated as $E_{RHE} = E_{Ag/AgCl} + 0.0591 pH + 0.197$.

The schematic diagram of the flow cell is depicted in Supplementary Fig. S14. Unlike the H-cell, the carbon paper used was a carbon paper with a gas diffusion layer. During the reaction, the electrolyte (0.1 M $KHCO_3$ with 50 mM $NaNO_3$, 30 mL) was passed through the reactor at a rate of 5 mL min^{-1} and the flow rate of carbon dioxide gas was 30 mL min^{-1}.

The detection methods for ammonia (NH_3), urea, H_2, CO and CO_2 concentrations were consistent with previous publications of our group [24–26]. The Faraday efficiency (FE) and the yield of urea synthesis can be calculated as follows:

$$FE_{urea}(\%) = \frac{16 \times F \times c_{urea} \times V}{60.06 \times Q} \times 100$$

$$Yield\quad rate_{urea} = \frac{c_{urea} \times V}{t \times m_{cat}}$$

where F (96485 C mol^{-1}) is Faraday constant, Q (C) is the electricity, C_{urea} (ppm) is the concentration of urea generated, V (L) is the volume of electrolyte, t (h) is the reduction time, and m_{cat} (g) is the loaded mass of the catalyst.

2.4. Operando SR-FTIR measurements

Surface-enhanced infrared absorption spectroscopy (SEIRAS) with attenuated total reflection (ATR) was used to detect intermediates in the reaction process. For the electrochemical ATR-SEIRAS measurements, a Thermo Nicolet 8700 spectrometer equipped with an MCT detector cooled with liquid nitrogen was used. Gold thin films (~60 nm) were chemically deposited on Si prisms according to the "two-step wet method". Prior to the chemical deposition of gold, the surface of the Si prism for IR reflection was polished with a diamond suspension and cleaned after ultrasonication in water. The prisms were then immersed in piranha solution (7:3 by volume of 98 % H_2SO_4 and 30 % H_2O_2) for 2 h. Then, the pretreated prisms were immersed in the mixture of the Au-plated solution (0.015 M $NaAuCl_4·2 H_2O$ + 0.15 M Na_2SO_3 + 0.05 M $Na_2S_2O_3·5 H_2O$ + 0.05 M NH_4Cl and a 2 wt% hydrofluoric acid solution in 1:2 vol ratio; T = 60 °C) for 1 min, rinsed with deionized water, and dissolved the Au film with aqua regia. The operating conditions of the second chemically depositing Au are basically the same as the first depositing conditions, except that the time is extended to 90 s. After chemical deposition of gold, the prisms were rinsed with ultrapure water and dried by air. 30 μL of ink was deposited and dried on the gold film working electrode, and the ink-coated prisms were then assembled into a homemade spectro-electrochemical cell as the working electrode with Ag/AgCl as reference, introduced through a Luggin capillary near the working electrode, and a Pt mesh (1 cm × 1 cm) as counter electrode. The electrochemical C-N coupling tests were tested in an aqueous solution consisted of 0.1 M $KHCO_3$ and 50 mM $NaNO_3$, with a constant CO_2 flow (30 mL min^{-1}) and controlled by a CHI electrochemical workstation (CHI 630E). The cathodic potential was swept from –1.1 V to –1.7 V vs. RHE every 100 mV. As a contrast, the CO_2RR tests were carried out in a 0.1 M $KHCO_3$ aqueous solution with a constant CO_2 flow (30 mL min^{-1}). And, the NO_3RR tests were performed in

a 50 mM $NaNO_3$ aqueous solution with Ar flow. All spectra were expressed as $\frac{\Delta R}{R} = \frac{E_s - E_R}{E_R}$, with Es and E_R representing the sample and reference spectra, respectively. If not specifically mentioned, the spectral resolution of all measurements is 4 cm^{-1}.

2.5. In-situ Raman spectroscopy

The in-situ Raman measurement setup consists of a Raman microscope, an in-situ Raman cell and an electrochemical workstation. The in-situ Raman chamber is designed of PTFE with a quartz window between the sample and the objective. The working electrode (carbon substrate) is in close contact with the graphite electrode to ensure conductivity. Graphite rods and Ag/AgCl are used as counter and reference electrodes, respectively. During the reaction, the electrolyte (0.1 M $KHCO_3$ with 50 mM $NaNO_3$, 30 mL) was passed through the in-situ Raman cell at a rate of 5 mL min^{-1}, and the flow rate of CO_2 gas was 15 mL min^{-1}. The cathodic potential was set from –0.6 V to –1.7 V vs. RHE every 200 mV. As a contrast, the CO_2RR tests were carried out in a 0.1 M $KHCO_3$ aqueous solution with a constant CO_2 flow (15 mL min^{-1}). The excitation wavelength was 632 nm from a He-Ne laser. The collection time was 0.5 s for these Cu_2O samples.

2.6. Computational method

All the DFT calculations were carried out via the Vienna ab initio simulation package (VASP). The projector augmented wave (PAW) approach was employed to describe the ion-electron interactions. The Exchange–correlation effects were treated by Perdew-Burke-Ernzerhof (PBE) functional within the framework of the generalized gradient approximation (GGA). A vacuum space of 20 Å was set along the direction perpendicular to the plane of the layer to avoid interactions between adjacent periodic images. The cutoff energy for geometrical optimization was set to be 550 eV, and the Brillouin zone was sampled with $3 \times 3 \times 1$. All the structures were relaxed until the energy and force reaching to the convergence criteria of 10^{-5} eV and 0.01 eV/Å. Given the possibility of hydrogen bonding, the van der Waals (vdW) interactions were described at the DFT-D3 level (including D3 version of Grimme's dispersion). Spin-polarized were also considered for the systems containing the unpaired electrons. To corrected the Coulomb interaction of D-orbital electrons, the DFT+U method proposed by Dudarev et al. was used. A value of $U_{eff} = 6$ eV was applied to the Cu-3d state according to the value used in the previous reports.

The Cu_2O (100) and (110) surfaces were modeled with a (2×2) supercell, which is cleaved from the optimized Cu_2O bulk unit cell. Typically, the possible terminated surface contains O, Cu and Cu+O-terminate types. But the O-terminated surfaces is more stable for (100)
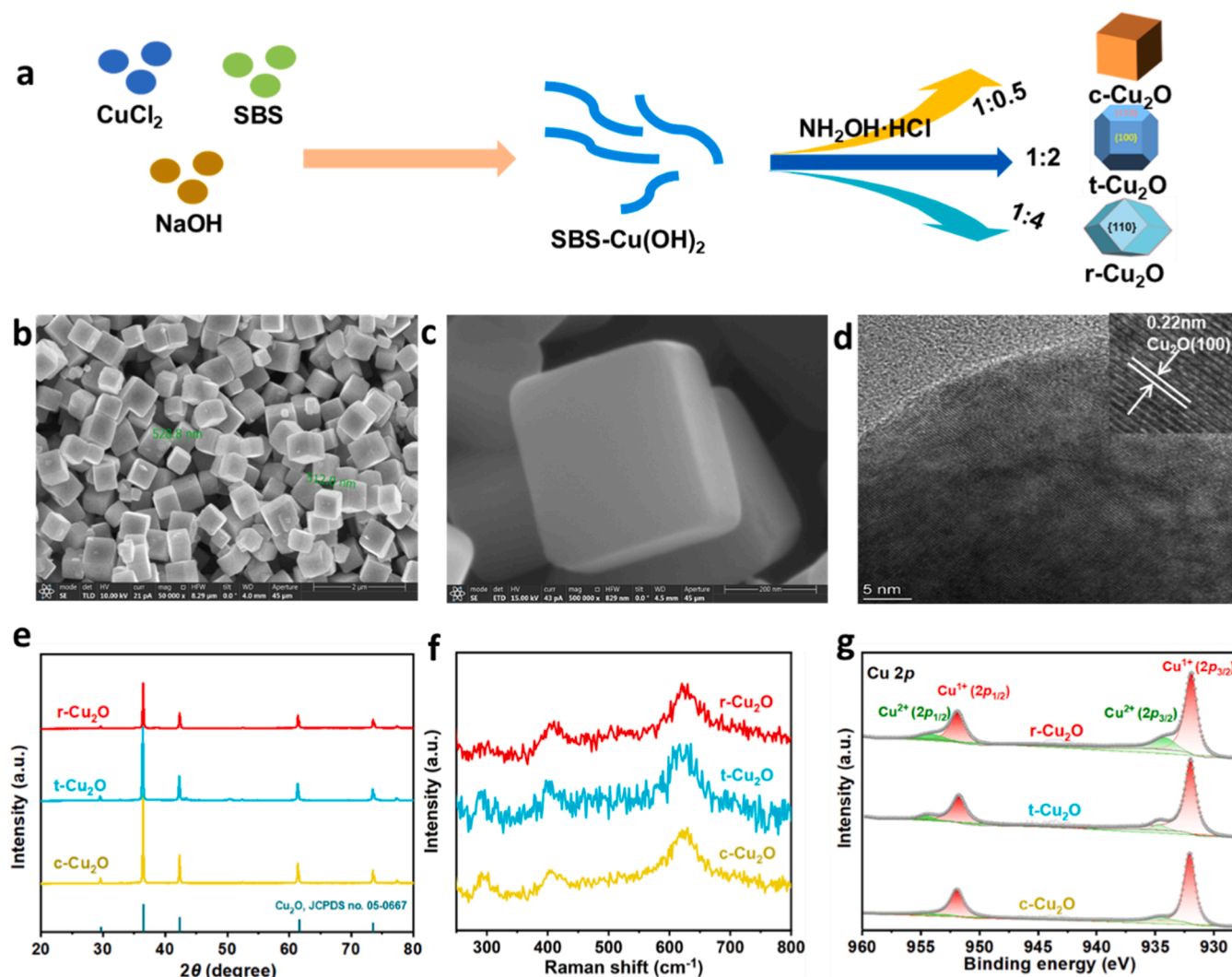

Fig. 1. Structural characterization of different Cu_2O NCs. **a)** Schematic for preparation of Cu_2O by the reductant-controlling method. SEM images of **b)** and **c)** c-Cu_2O, **d)** TEM images of c-Cu_2O. **e)** XRD patterns. **f)** Raman spectra. **g)** Cu 2p XPS curves.

surfaces, while (110) surface is thermodynamically more favorable with Cu+O-terminate. Combined with that O-defect is a common defect in metallic oxides, we built an O-terminated Cu_2O (100) model with O-defect to expose the catalytic active sites of Cu in the second layer. In the adsorption calculations on the (100) model, the bottom four layers were kept fixed, while the other layers were fully relaxed. For the (110) model, only the bottom two layers were fixed. To improve convergence for the relaxation of the polar surface described above, we have included the dipole correction in the normal direction.

3. Results and discussions

3.1. Characterization of electrocatalytic materials

The hydroxylamine hydrochloride reduction method was used for the preparing of facet-dependent Cu_2O nanoparticles (NCs) by altering the proportion of the precursor (Fig. 1a and S2). In this work, three types of Cu_2O samples were prepared: c-Cu_2O with a cubic nano-structure (Fig. 1b, c) enclosed by six (100) planes, t-Cu_2O exhibiting a polyhedral morphology (Fig. S3a, c) with six square (100) faces in addition to twelve (110) faces, and r-Cu_2O consisting mainly of a rhombic dodecahedral morphology (Fig. S3b, d) exposed with twelve Cu_2O (110)

planes. X-ray diffraction characterization was firstly used to analyze the detailed crystal structure of these Cu_2O NCs. Typically, the five diffraction peaks at 2θ of 29.55, 36.42, 42.30, 61.34 and 73.53° were assigned to the Cu_2O (110), (111), (200), (220) and (311) planes, respectively, which are consistent with the Cu_2O crystal structure (Fig. 1e) [27,28]. The structural information of these Cu_2O NCs was also investigated by Raman spectroscopy (Fig. 1f), which clearly reveals the characteristic phonon frequencies of crystalline Cu_2O (416 cm^{-1}, and 635 cm^{-1}) in all samples [29,30]. The Raman spectrum also detected a weak CuO Raman peak at 292 cm^{-1}, which may be due to the inevitable partial oxidation [30–32]. Furthermore, the morphology of the three Cu_2O NCs was confirmed by TEM analysis, as seen in Fig. 1d and S4. The TEM images near the particle edges show distinct lattice edges with D-spacings of 2.2 and 2.9 Å, corresponding to the (100) and (110) lattice planes of Cu_2O. Finally, XPS was used to identify the surface electronic states of the three Cu_2O NCs. The peaks of Cu_2O NCs at 951.7 and 931.9 eV were attributed to Cu $2p_{1/2}$ and $2p_{3/2}$, respectively, confirming the presence of Cu(I) in Cu_2O (Fig. 1g) [33].

3.2. Electrocatalytic urea synthesis
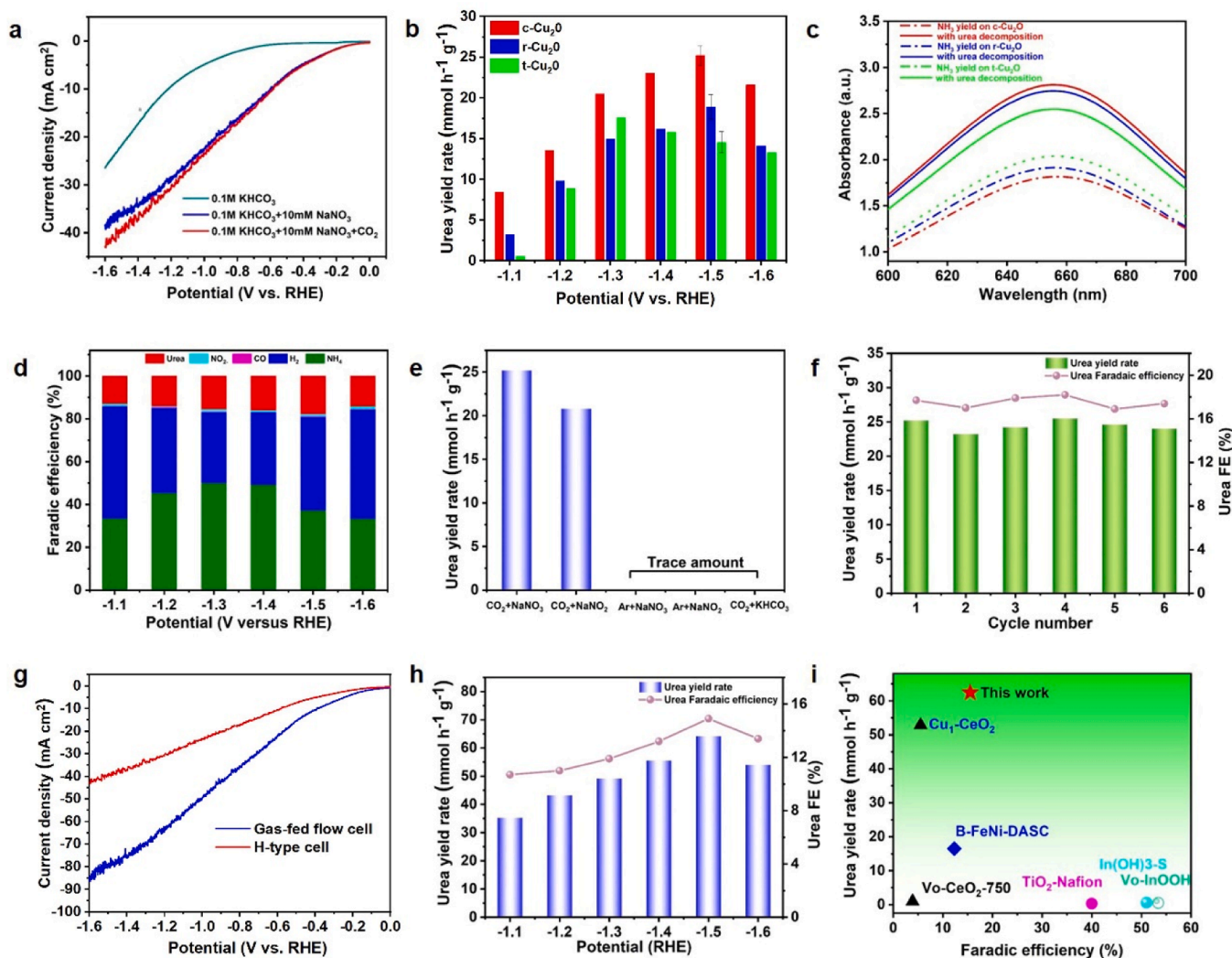
The electrochemical experiments were performed using the

Fig. 2. Electrocatalytic performance of urea synthesis. **a)** LSV curves of c-Cu_2O at $KHCO_3$ solution, mixed $NaNO_3$ and $KHCO_3$ solution, and mixed CO_2-saturated $NaNO_3$ and $KHCO_3$ solution. **b)** Urea yield rate. **c)** UV–vis absorption spectra for NH_3 and urea quantification. **d)** Faradic efficiencies. **e)** The control experiment was carried at different reaction feedstocks. **f)** Stability tests of c-Cu_2O at –1.5 V versus RHE. **g)** LSV curves for 45-nm c-Cu_2O in H-type cell and Gas-fed flow cell. **h)** Urea yield rate of 45 nm-sized cubic Cu_2O in the flow cell. **i)** Urea yield rate of 45 nm-sized cubic Cu_2O compared with those of other state-of-the-art urea yield rate.

chronoamperometry method at a fixed potential in a typical three-electrode configuration of an H-cell reactor (Fig. S5). The yield rate of urea produced was quantified by urease decomposition method (Fig. 2c, S6, S7), which can avoid the interference of coexisting byproducts (NO_2^-) [25]. Firstly, the potential performance of urea electrosynthesis was evaluated using Linear scanning voltammetry (LSV) method (Fig. 2a). Clearly, c-Cu_2O exhibited the highest current density in CO_2-saturated NO_3^- and HCO_3^- mixed solutions relative to simple HCO_3^- solutions or a mixture of NO_3^- and HCO_3^-, indicating that a C-N coupling reaction occurred. Then, the catalyst mass loading on carbon paper was optimized according to the produced urea yield rate as displayed in Fig. S8. At last, the electrocatalysis tests were carried out at applied potentials of –1.1 V to –1.7 V versus reversible hydrogen electrode (RHE) with an interval of 0.1 V. The highest value of urea yield of c-Cu_2O reached 25.2 mmol·h^{-1}·g^{-1} at –1.5 V (vs. RHE) with a urea FE of 17.7 % (Fig. 2b, d). Notably, the yield of c-Cu_2O was almost 1.3 and 1.7 times higher than that of r-Cu_2O and t-Cu_2O at the same potential, indicating that the Cu_2O (100) facets contributes to the electrocatalysis of C-N coupling into urea. Moreover, as shown in the linear scanning voltammetry (LSV) curves in Fig. S9a, the current density of c-Cu_2O is greater compared to t-Cu_2O and r-Cu_2O, suggesting the higher activity of the c-Cu_2O catalyst. Fig. S9b and S10 show the j_{urea} and FE_{urea} of c-Cu_2O, t-Cu_2O and r-Cu_2O at different potentials. The FE_{urea} of c-Cu_2O catalyst exceeds 12 % over a wide potential range of –1.1 to –1.6 V relative to RHE, and reaches an optimum value of 17.72 % at –1.5 V relative to RHE. It can also be found in Fig. S10 that the optimum FE_{urea} for t-Cu_2O and r-Cu_2O at –1.5 V relative to RHE are14.34 % and 16.53 %, respectively. The j_{urea} on c-Cu_2O increases with more negative potentials applied and reaches 7.2 mA cm^{-2} at –1.5 V relative to RHE, which is much larger than that of t-Cu_2O and r-Cu_2O. Then, control experiments were performed in 0.1 M $KHCO_3$ or Ar, which resulted in no urea production. Urea products were formed only when both nitrate and CO_2 were used as feedstocks (Fig. 2e), suggesting that urea does come from the co-electrolysis of NO_3^- and CO_2. After six consecutive cycles at –1.5 V, no obvious decay in urea yield and FE was observed (Fig. 2f), and the crystalline structure of c-Cu_2O remained after long-term testing (Fig. S11), confirming the excellent electrochemical and structural stability of c-Cu_2O.

The optimal particle size of Cu_2O (100) facets was investigated to further improve the urea yield. Nano-Cu_2O samples with average particle sizes of 45 and 69 nm were synthesized, as illustrated in Fig. S12 and S13. The variation of the half-peak width at 36.4° in XRD patterns also further supports the SEM results. Due to the highest active specific surface area of the ultra-small c-Cu_2O nanocrystals, the 45 nm-sized c-Cu_2O nanocrystals showed the highest urea yield of 34.6 mmol·h^{-1}·g^{-1} at –1.5 V. However, the low solubility of CO_2 in aqueous media severely limits the current density of the H-cell. Therefore, we further used a gas-fed flow cell equipped with a gas diffusion electrode (GDE) to evaluate the urea yield (Fig. S14). As shown in Fig. 2g, the current density of 45 nm-sized c-Cu_2O in the flow cell significantly exceeds that of H-cell, indicating that CO_2 diffuses more rapidly through the gas phase to the catalyst in the flow cell apparatus. In the flow cell apparatus, the urea yield remained above 35 mmol·h^{-1}·g^{-1} with a maximum value of 64.2 mmol·h^{-1}·g^{-1} in the potential range of –1.1 to –1.6 V versus RHE, which exceeds most previous reports (Fig. 2h, i, and Table S1).

3.3. C-N coupling mechanistic studies

Firstly, the effect of different crystal faces of Cu_2O on the electrochemical C-N coupling reaction path was investigated by studying the variation of the main products (urea, NH_3, and H_2) as a function of the potential. As shown in Fig. S10, the faraday efficiency of NH_3, urea and H_2 produced by the three samples showed similar trends, with FE_{NH3} and FE_{urea} initially increasing sharply and then decreasing with increasing applied potential, while the FE_{H2} showed a clear opposite trend with increasing potential. This trend suggested that HER and NO_3RR inevitably compete strongly with the desirable urea formation at negative potentials, which resulted in the low urea faraday efficiency. For the HER, there is a greater tendency to produce H_2 on the (100) and (110) mixing facets of Cu_2O, which may be due to the charge transfer between the (110) and (100) surfaces, as observed in the previous research [34]. The higher HER competition reaction resulted in the lowest urea yield of t-Cu_2O. It is worth mentioning that as the applied voltage decreases, the competitive of the HER decreases. This was confirmed by the observation that the urea yield of t-Cu_2O is higher than that of r-Cu_2O at a voltage of –1.3 V (Fig. 2b). The linear scanning voltammetry (LSV) curves for the three catalysts also showed that the j_{urea} of t-Cu_2O is larger than that of r-Cu_2O at the lower potential (Fig. S9), indicating the higher urea yield of t-Cu_2O compared to r-Cu_2O. As for the r-Cu_2O, the weaker adsorption of CO on the Cu_2O (110) facets due to the lower Fermi level on the Cu_2O (110) facets would allow *NH to occupy more active sites and promote more production of NH_3 [35, 36]. In contrast, the adsorption capacity of CO is stronger on the Cu_2O (100) facets than that on the Cu_2O (110) facets, as indicated by DFT calculation [35,37]. This would subsequently facilitate C-N coupling and produce urea products. A summary of the influence of the crystal facets on the sub-reaction path of the C-N coupling reaction is shown in the Fig. S15.

Then, the key reaction intermediates were further identified by electrochemical operando ATR-SEIRAS spectroscopy. As seen in Fig. 3c, *NHCO (1662 cm^{-1}), *CN (1477 cm^{-1}), *CN (1403 cm^{-1}), and *OCO (1370 cm^{-1}) were detected at the reduction potential using CO_2 and nitrite as feedstock [21,24,39], indicating that nitrate and CO_2 can be co-activated on the catalyst, which is consistent with our goal of constructing a cooperative operation on the sub-reactive sites of NO_3RR and CO_2RR. Moreover, the vibrational intensity of *NHCO (1662 cm^{-1}) gradually increases with the increase of the negative potential, reaching a maximum at –1.5 V and then gradually decreases (Fig. S18). The evolution of *NHCO species is consistent with the electrochemical test results, which implies that the formation of intermediate species, especially *NHCO, is closely related to the production of urea [24]. As compared, the operando ATR-SEIRAS spectroscopy was also carried out in simple NO_3^- solutions (NO_3RR) or a mixture of CO_2 gas and HCO_3^- (CO_2RR), as shown in Fig. 3d and e. During CO_2RR, a CO-related peak at ~2035 cm^{-1} was observed [40]. This signal was not observed in the co-electrolysis reaction, which may be due to the fact that *CO is quickly involved in the subsequent C-N reaction, resulting in a weak signal. In addition, no C-N intermediate reactants were detected in both NO_3RR and CO_2RR, which is further evidence that urea is indeed derived from the co-electrolysis of CO_2 and NO_3^-. Furthermore, the in-situ Raman spectroscopy was used to verify the intermediate products of the C-N coupling reaction on the Cu_2O catalyst (Fig. 3f). At the reduction potential, Raman measurements showed a prominent emergent peak at 1053 cm^{-1}, corresponded to the adsorbed carbonate species of *CO_3^{2-} (Fig. 3a and f) [38]. The CO_3^{2-} signal first increases and then decreases from – 1.2 V to – 1.6 V, which is in good agreement with the urea yield. These findings suggest that the CO_2RR promotes the C-N coupling reaction, while the HER and NO_3RR compete with the C-N reaction and inhibit the urea synthesis. Meanwhile, a CO-related peak at ~2070 cm^{-1} (CO stretching) appeared during CO_2RR (Fig. 3g) [38]. This observation is consistent with the results of operando ATR-SEIRAS, indicating that the *CO intermediates is involved in the C-N coupling reaction. Therefore, a coupling mechanism was proposed on this basis: the Cu_2O catalyst firstly reacts with NO_3^- to produce more *NH intermediates, then the *CO intermediates react with the adsorbed *NH to produce the urea intermediate *NHCO, and finally urea is produced in high yield.

3.4. The active sites of c-Cu_2O (100) facets for C-N coupling

In our discussion so far, the question of whether the catalytic activity of Cu_2O NPs is an intrinsic property of these NPs or arises from the metallic Cu NPs generated on the surface of Cu_2O NPs during C-N coupling has not been investigated. To explore this issue, the properties
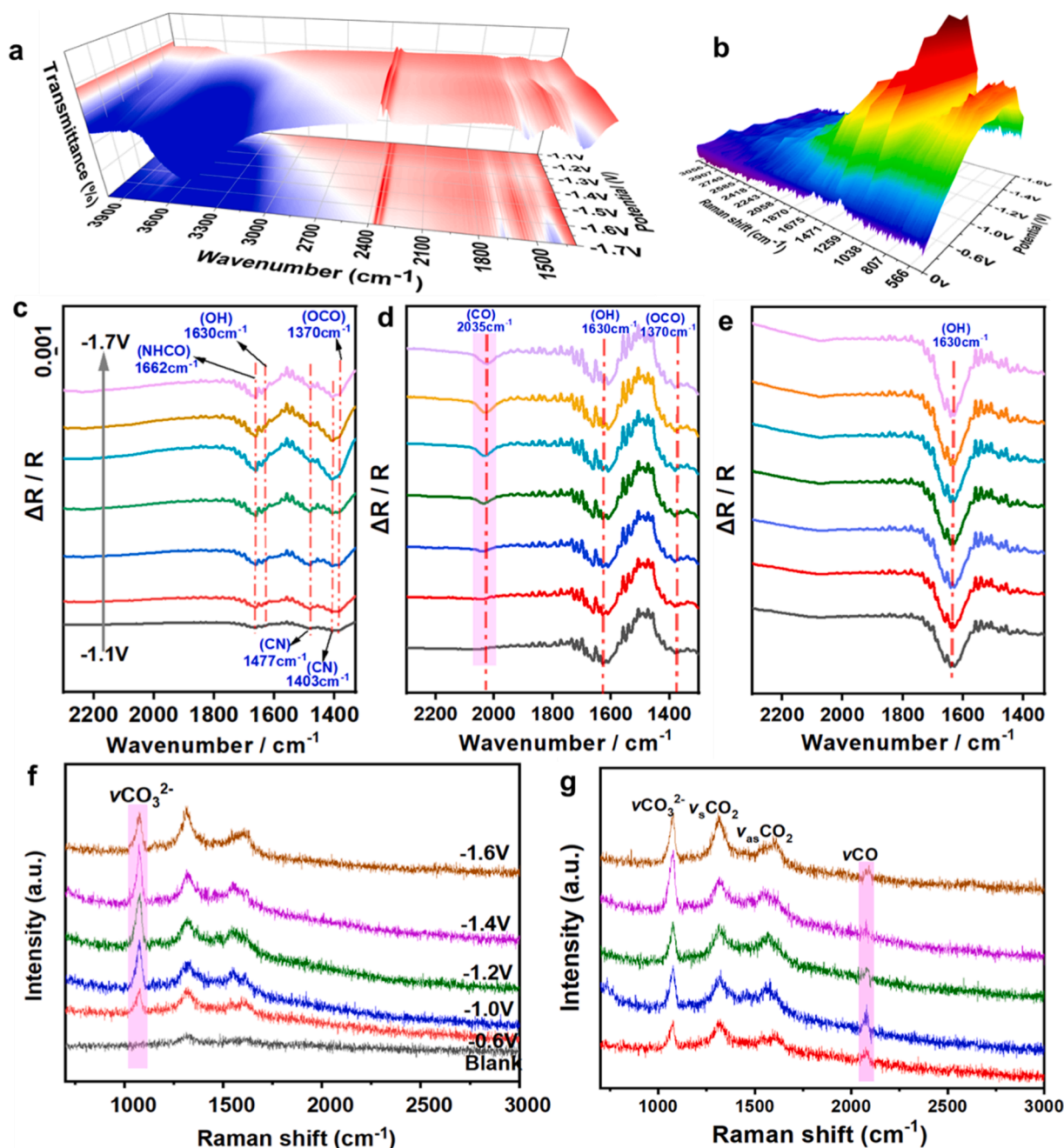
Fig. 3. C-N coupling mechanistic studies. **a)** Operando ATR-SEIRAS spectroscopy for 45 nm-Cu_2O during the electrocoupling of NO_3^- and CO_2. **b)** In-situ Raman spectroscopy. **c)** Infrared signals in the range of 2300–1300 cm^{-1} during the electrocoupling of NO_3^- and CO_2. **d)** Infrared signals during CO_2RR, **e)** Infrared signals during NO_3RR, **f)** Raman signals during the electrocoupling of NO_3^- and CO_2, **g)** Raman signals during the electrocoupling of CO_2RR.

of c-Cu_2O before and after the C-N coupling reaction were comparatively analyzed using in-situ Raman, XPS, and UV–vis. In-situ Raman spectroscopy revealed that the c-Cu_2O samples were present in the intrinsic phase of Cu_2O under the electrocatalytic reaction conditions (potentials greater than ~−1.6 V_{RHE}), identified by the peaks at ~310 cm^{-1} (second-order overtone mode $2\Gamma_{15}^{(1)-}$), and ~410 cm^{-1} (four-phonon mode $3\Gamma_{12}^- + \Gamma_{25}^-$) (Fig. 4a) [30,41]. We also found that the intensity of these Raman signals decreased under the operating conditions, suggesting partial reduction of Cu_2O to metallic Cu. Moreover, the Cu_2O retained the characteristic Raman modes at different potentials, suggesting that the Cu^0/Cu^+ interfaces in Cu_2O play a key role in the urea synthesis. From the UV-Vis spectrum (Fig. 4b), it can be found that the Cu_2O characteristic peak (~460 nm) is significantly red-shifted after the

electrocatalytic C-N coupling reaction, indicating an increase in the structural defects and consequently an increase in the density of Cu^0 species on the c-Cu_2O surface. [42–44]. In addition, XPS spectra confirmed that the c-Cu_2O sample consisted mainly of Cu^+ during the electrocatalysis tests, as indicated by the peak of 570.5 eV. Moreover, the percentage of Cu^0 species increased from 9.1 % to 16.3 % during the electrocatalytic tests, as determined by the intensity variation of the peak at 568.4 eV (Fig. 4c) [45]. Based on these results, we conclude that Cu^+ is the active center of the Cu_2O catalyst, which promotes CO_2 activation and C-N coupling through synergistic interactions with Cu^0, as seen in Fig. S19.

Finitely, DFT calculation was used to verify the mechanism of C-N coupling on these active sites (Fig. 4d, e, and R20–22). The reaction path
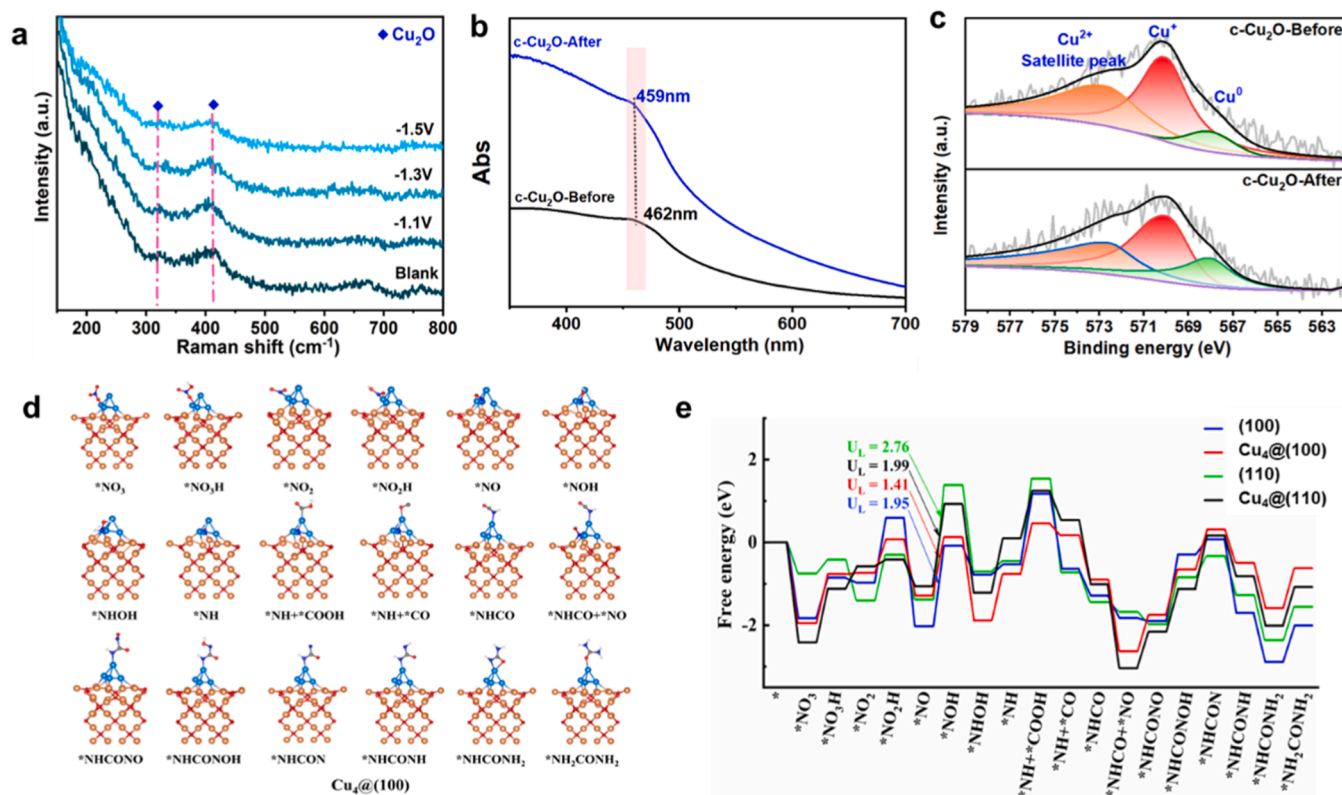
Fig. 4. a) In-situ Raman spectroscopy of c-Cu₂O during reactions. **b)** UV–vis spectroscopy, **c)** Cu LMM AES spectra of c-Cu₂O before and after reactions. **d)** The corresponding configurations of intermediates involving in urea formation on Cu_4 @ (100) slab. **e)** DFT calculation of the free energy profiles.

on the Cu-Cu₂O (100) starting from NO_3^- are presented in Fig. 4e, and the corresponding adsorption configurations are displayed in Fig. 4d. The formation of urea reacted in the *NH+ *CO path, which means that the *CO intermediate generated from CO₂RR combined with the *NH intermediate produced from NO₃RR. Overall, there is no obvious difference between the reaction pathways on the (100) and (110) surfaces except for the intensity of adsorption of the intermediates. Both of the four surfaces result in the same rate-limiting step of *NO→*NOH, but the Cu_4 @ (100) surface (U_L=1.41 eV) is more thermodynamically favorable for the formation of *NOH than other surfaces. The huge disparity in U_L induced the superior catalytic activity in c-Cu₂O. In addition, the thermodynamic spontaneous process in the first C-N coupling (*NH+CO→*NHCO) and the second C-N coupling (*NHCO+NO→*NHCONO) ensured the forward formation of urea. Moreover, the Cu_4 @ (100) surface exhibits a lower reaction U_L compared to the pure (100) surface, which further suggests that Cu^0/Cu^+ acts as a dual active site for the C-N coupling reaction.

4. Conclusions

The determination of the active sites and mechanisms of urea synthesis by electrochemical methods is important for the subsequent design of efficient electrocatalysts. Using a model Cu₂O catalyst, the facet-dependent activity origins for selective electrocatalytic synthesis of urea was probed. It was found that Cu^+ is the main active site of the Cu₂O (100) facet, which can promote CO₂ activation and C-N coupling through synergistic interaction with Cu^0. The C-N coupling reaction mechanism was verified by taking the advantage of operando ATR-SEIRAS and DFT calculation. And benefitting from the reduced energy barrier of hydrogenation *NO on the Cu-Cu₂O (100) facet, the Cu-Cu₂O (100) facet exhibited superior urea synthesis performance.

CRediT authorship contribution statement

Jiamin Zhao: Methodology, Data curation, Project administration. **Ying Yuan:** Validation, Formal analysis. **Fei, Zhao:** Software. **Wei Han:** Supervision. **Qing Yuan:** Data curation. **Meimei Kou:** Validation. **Jinsheng Zhao:** Writing-review. **Chen Chen:** Writing-review & editing. **Shuangyin Wang:** Supervision, Writing - review & editing.

Declaration of Competing Interest

The authors declare that they have no known competing financial interests or personal relationships that could have appeared to influence the work reported in this paper.

Data Availability

Data will be made available on request.

Acknowledgments

Appendix A. Supporting information

References

[1] J.W. Erisman, M.A. Sutton, J. Galloway, Z. Klimont, W. Winiwarter, How a century of ammonia synthesis changed the world, Nat. Geosci. 1 (2008) 636–639.

[2] C. Smith, A.K. Hill, L. Torrente-Murciano, Energy Environ. Sci. 13 (2020) 331–344.

[3] S.L. Foster, S.I.P. Bakovic, R.D. Duda, S. Maheshwari, R.D. Milton, S.D. Minteer, M. J. Janik, J.N. Renner, L.F. Greenlee, Catalysts for nitrogen reduction to ammonia, Nat. Catal. 1 (2018) 490–500.

[4] G. Soloveichik, Electrochemical synthesis of ammonia as a potential alternative to the Haber-Bosch process, Nat. Catal. 2 (2019) 377–380.

[5] N. Cao, Y. Quan, A. Guan, C. Yang, Y. Ji, L. Zhang, G. Zheng, Oxygen vacancies enhanced cooperative electrocatalytic reduction of carbon dioxide and nitrite ions to urea, J. Colloid Interface Sci. 577 (2020) 109–114.

[6] Y. Huang, Y. Wang, Y. Liu, A. Ma, J. Gui, C. Zhang, Y. Yu, B. Zhang, Unveiling the quantification minefield in electrocatalytic urea synthesis, Chem. Eng. J. 453 (2023), 139836.

[7] G. Qing, R. Ghazfar, S.T. Jackowski, F. Habizadeh, M.M. Ashtiani, C.P. Chen, M. R. Smith III, T.W. Hamann, Recent advances and challenges of electrocatalytic N$_2$ reduction to ammonia, Chem. Rev. 120 (2020) 5437–5516.

[8] X. Liu, P.V. Kumar, Q. Chen, L. Zhao, F. Ye, X. Ma, D. Liu, X. Chen, L. Dai, C. Hu, Carbon nanotubes with fluorine-rich surface as metal-free electrocatalyst for effective synthesis of urea from nitrate and CO$_2$, Appl. Catal. B 316 (2022), 121618.

[9] J. Li, F. Wei, C. Dong, Z. Wang, Z. Xiu, X. Han, Recent progress of inorganic metal-based catalysts in electrocatalytic synthesis of ammonia, Mater. Today Energy 21 (2021) 100766.

[10] C. Chen, X. Zhu, X. Wen, Y. Zhou, L. Zhou, H. Li, L. Tao, Q. Li, S. Du, T. Liu, D. Yan, C. Xie, Y. Zou, Y. Wang, R. Chen, J. Huo, Y. Li, J. Cheng, H. Su, X. Zhao, W. Cheng, Q. Liu, H. Lin, J. Luo, J. Chen, M. Dong, K. Cheng, C. Li, S. Wang, Coupling N$_2$ and CO$_2$ in H$_2$O to synthesize urea under ambient conditions, Nat. Chem. 12 (2020) 717–724.

[11] Y. Feng, H. Yang, Y. Zhang, X. Huang, L. Li, T. Cheng, Q. Shao, Te-doped Pd nanocrystal for electrochemical urea production by efficiently coupling carbon dioxide reduction with nitrite reduction, Nano Lett. 20 (2020) 8282–8289.

[12] M.T. Sabatini, L.T. Boulton, H.F. Sneddon, T.D. Sheppard, A green chemistry perspective on catalytic amide bond formation, Nat. Catal. 2 (2019) 10–17.

[13] M. Jouny, J.J. Lv, T. Cheng, B.H. Ko, J.J. Zhu, W.A. Goddard, F. Jiao, Formation of carbon-nitrogen bonds in carbon monoxide electrolysis, Nat. Chem. 11 (2019) 846–851.

[14] Z.J. Lv, J. Wei, W.X. Zhang, P. Chen, D. Deng, Z.J. Shi, Z. Xi, Direct transformation of dinitrogen: synthesis of N-containing organic compounds via N-C bond formation, Natl. Sci. Rev. 7 (2020) 1564–1583.

[15] Z. Li, P. Zhou, M. Zhou, H. Jiang, H. Li, S. Liu, H. Zhang, S. Yang, Z. Zhang, Synergistic electrocatalysis of crystal facet and O-vacancy for enhancive urea synthesis from nitrate and CO$_2$, Appl. Catal. B (2023), 122962.

[16] C. Tang, Y. Zheng, M. Jaroniec, S.Z. Qiao, Electrocatalytic refinery for sustainable production of fuels and chemicals, Angew. Chem. Int. Ed. 60 (2021) 19572–19590.

[17] C. Chen, N. He, S. Wang, Electrocatalytic C-N coupling for urea synthesis, Small Sci. 1 (2021), 2100070, https://doi.org/10.1002/smsc.202100070.

[18] G.W.K. Moore, S.E.L. Howell, M. Brady, X. Xu, K. McNeil, Anomalous collapses of Nares Strait ice arches leads to enhanced export of Arctic sea ice, Nat. Comm. 12 (2021) 1.

[19] J. Leverett, T. Tran-Phu, J.A. Yuwono, P. Kumar, C. Kim, Q. Zhai, C. Han, J. Qu, J. Cairney, A.N. Simonov, R.K. Hocking, L. Dai, R. Daiyan, R. Amal, Tuning the coordination structure of Cu-N-C Single atom catalysts for simultaneous electrochemical reduction of CO$_2$ and NO$_3$ to Urea, Adv. Energy Mater. 12 (2022), 2201500.

[20] M. Yuan, J. Chen, Y. Bai, Z. Liu, J. Zhang, T. Zhao, Q. Wang, S. Li, H. He, G. Zhang, Unveiling electrochemical urea synthesis by co-activation of CO$_2$ and N$_2$ with Mott-Schottky heterostructure catalysts, Angew. Chem. Int. Ed. 60 (2021) 10910–10918.

[21] C. Lv, L. Zhong, H. Liu, Z. Fang, C. Yan, M. Chen, Y. Kong, C. Lee, D. Liu, S. Li, J. Liu, L. Song, G. Chen, Q. Yan, G. Yu, Selective electrocatalytic synthesis of urea with nitrate and carbon dioxide, Nat. Sustain. 4 (2021) 868–876.

[22] Z. Tao, C.L. Rooney, Y. Liang, H. Wang, Accessing organonitrogen compounds via C-N coupling in electrocatalytic CO$_2$ reduction, J. Am. Chem. Soc. 143 (2021) 19630–19642.

[23] X. Wei, X. Liu, X. Zhu, S. Bo, L. Xiao, C. Chen, T.T.T. Nga, Y. He, M. Qiu, C. Xie, D. Wang, Q. Liu, F. Dong, C.L. Dong, X.Z. Fu, S. Wang, Dynamic reconstitution between copper single atoms and clusters for electrocatalytic urea synthesis, Adv. Mater. 35 (2023), 230020.

[24] X. Zhang, X. Zhu, S. Bo, C. Chen, M. Qiu, X. Wei, N. He, C. Xie, W. Chen, J. Zheng, P. Chen, S.P. Jiang, Y. Li, Q. Liu, S. Wang, Identifying and tailoring C-N coupling site for efficient urea synthesis over diatomic Fe-Ni catalyst, Nat. Commun. 13 (2022) 5337.

[25] X. Wei, X. Wen, Y. Liu, C. Chen, C. Xie, D. Wang, M. Qiu, N. He, P. Zhou, W. Chen, J. Cheng, H. Lin, J. Jia, X.Z. Fu, S. Wang, Oxygen vacancy-mediated selective C-N coupling toward electrocatalytic urea synthesis, J. Am. Chem. Soc. 144 (2022) 11530–11535.

[26] Y. Liu, X. Tu, X. Wei, D. Wang, X. Zhang, W. Chen, C. Chen, S. Wang, C-bound or O-bound surface: which one boosts electrocatalytic urea synthesis? Angew. Chem. Int. Ed. 135 (2023), e202300387.

[27] W.C. Huang, L.M. Lyu, Y.C. Yang, M.H. Huang, Synthesis of Cu$_2$O nanocrystals from cubic to rhombic dodecahedral structures and their comparative photocatalytic activity, J. Am. Chem. Soc. 134 (2012) 1261–1267.

[28] Y. Jiang, T. Xia, L. Shen, J. Ma, H. Ma, T. Sun, F. Lv, N. Zhu, Facet-dependent Cu$_2$O electrocatalysis for wearable enzyme-free smart sensing, ACS Catal. 11 (2021) 2949–2955.

[29] Y.K. Hsu, C.H. Yu, Y.C. Chen, Y.G. Lin, Fabrication of coral-like Cu$_2$O nanoelectrode for solar hydrogen generation, J. Power Sources 242 (2013) 541–547.

[30] Y. Mao, J. He, X. Sun, W. Li, X. Lu, J. Gan, Z. Liu, L. Gong, J. Chen, P. Liu, Y. Tong, Electrochemical synthesis of hierarchical Cu$_2$O stars with enhanced photoelectrochemical properties, Electrochim. Acta 62 (2012) 1–7.

[31] W. Wen, P. Yan, W. Sun, Y. Zhou, X.Y. Yu, Metastable phase Cu with optimized local electronic state for efficient electrocatalytic production of ammonia from nitrate, Adv. Funct. Mater. 33 (2023), 2212236.

[32] Y.K. Hsu, C.H. Yu, Y.C. Chen, Y.G. Lin, Fabrication of coral-like Cu$_2$O nanoelectrode for solar hydrogen generation, J. Power Sources 242 (2013) 541–547.

[33] H. Jung, S.Y. Lee, C.W. Lee, M.K. Cho, D.H. Won, C. Kim, H.S. Oh, B.K. Min, Y. J. Hwang, Electrochemical fragmentation of Cu$_2$O nanoparticles enhancing selective C-C coupling from CO$_2$ reduction reaction, J. Am. Chem. Soc. 141 (2019) 4624–4633.

[34] H.L. Skriver, N.M. Rosengaard, Surface energy and work function of elemental metals, Phys. Rev. B 46 (1992) 7157–7168.

[35] Y. Gao, Q. Wu, X. Liang, Z. Wang, Z. Zheng, P. Wang, Y. Liu, Y. Dai, M. H. Whangbo, B. Huang, Cu$_2$O nanoparticles with both {100} and {111} facets for enhancing the selectivity and activity of CO$_2$ electroreduction to ethylene, Adv. Sci. 7 (2020), 1902820.

[36] Y. Wang, W. Zhou, R. Jia, Y. Yu, B. Zhang, Unveiling the activity origin of a copper-based electrocatalyst for selective nitrate reduction to ammonia, Angew. Chem. Int. Ed. 59 (2020) 5350–5354.

[37] Y. Wang, C. Wang, M. Li, Y. Yu, B. Zhang, Nitrate electroreduction: mechanism insight, in situ characterization, performance evaluation, and challenges, Chem. Soc. Rev. 50 (2021) 6720–6733.

[38] Y. Zhao, X.G. Zhang, N. Bodappa, W.M. Yang, Q. Liang, P.M. Radjenovica, Y. H. Wang, Y.J. Zhang, J.C. Dong, Z.Q. Tian, J.F. Li, Elucidating electrochemical CO$_2$ reduction reaction processes on Cu (hkl) single-crystal surfaces by in situ Raman spectroscopy, Energ. Environ. Sci. 15 (2022) 3968–3977.

[39] S.K. Geng, Y. Zheng, S.Q. Li, H. Su, X. Zhao, J. Hu, H.B. Shu, M. Jaroniec, P. Chen, Q.H. Liu, S.Z. Qiao, Nickel ferrocyanide as a high-performance urea oxidation electrocatalyst, Nat. Energy 6 (2021) 904–912.

[40] Y. Xu, C. Li, Y. Xiao, C. Wu, Y. Li, Y. Li, J. Han, Q. Liu, J. He, Tuning the selectivity of liquid products of CO$_2$RR by Cu-Ag alloying, ACS Appl. Mater. Interfaces 14 (2022) 11567–11574.

[41] Z. Wang, V. Pischedda, S.K. Saxena, P. Lazor, X-ray diffraction and Raman spectroscopic study of nanocrystalline CuO under pressures, Solid State Commun. 121 (2002) 275–279.

[42] R.R. Rao, S. Corby, A. Bucci, M. García-Tecedor, C.A. Mesa, J. Rossmeisl, S. Giménez, J. Lloret-Fillol, I.E.L. Stephens, J.R. Durrant, Spectroelectrochemical analysis of the water oxidation mechanism on doped nickel oxides, J. Am. Chem. Soc. 144 (2022) 7622–7633.

[43] J.Y. Huang, M. Madasu, M.H. Huang, Modified semiconductor band diagrams constructed from optical characterization of size-tunable Cu$_2$O cubes, octahedra, and rhombic dodecahedra, J. Phys. Chem. C 122 (2018) 13027–13033.

[44] W.H. Ke, C.F. Hsia, Y.J. Chen, M.H. Huang, Synthesis of ultrasmall Cu$_2$O nanocubes and octahedra with tunable sizes for facet-dependent optical property examination, Small 12 (2016) 3530–3534.

[45] X. Chang, T. Wang, Z.J. Zhao, P. Yang, J. Greeley, R. Mu, G. Zhang, Z. Gong, Z. Luo, J. Chen, Y. Cui, G.A. Ozin, J. Gong, Tuning Cu/Cu$_2$O interfaces for the reduction of carbon dioxide to methanol in aqueous solutions, Angew. Chem. Int. Ed. 57 (2018) 15415–15419.